Biosensors and Bioelectronics 142 (2019) 111573

Contents lists available at ScienceDirect

Biosensors and Bioelectronics

journal homepage: www.elsevier.com/locate/bios

Recent advances in two-dimensional transition metal dichalcogenides for biological sensing

Huawen Hu[a,1], Ali Zavabeti[b,c,1], Haiyan Quan[a], Wuqing Zhu[a], Hongyang Wei[a], Dongchu Chen[a,*], Jian Zhen Ou[b,**]

[a] School of Materials Science and Energy Engineering, Foshan University, Foshan, Guangdong, 528000, China
[b] School of Engineering, RMIT University, Melbourne, Victoria, 3000, Australia
[c] College of Materials Science and Technology, Nanjing University of Aeronautics and Astronautics, Nanjing, Jiangsu, 211100, China

ARTICLE INFO

Keywords:
Two-dimensional nanomaterials
Transition metal dichalcogenides
Graphene
Preparation methods
Biosensing

ABSTRACT

Layered transition metal dichalcogenides (TMDs) are important members in the family of two-dimensional (2D) materials. The large surface-to-volume ratio, combined with the fascinating tunable electronic and optical properties, low toxicity, unique van der Waals layered structure, and engineerable surface structure, renders 2D TMDs highly valuable for next-generation biosensing applications. Herein, the recent progress in the development of 2D TMDs-based biosensors is comprehensively reviewed, with special focus on the implementation of the structural, electronic and optical properties of 2D TMDs in the realization of high-performance biosensors with different configurations for a wide spectrum of bioanalytes and bio-species. In addition, the comparison on biosensing performances with graphene as the currently most studied 2D candidate is critically discussed. Finally, future perspectives are provided along the development progress of 2D TMDs-based biosensors which are currently undergoing an intense study. This work will lead researchers to explore more novel sensing candidates within the category of TMDs with exotic chemical composition, structure, morphologies, dimensionalities, and properties.

1. Introduction

As one of the most popular graphene analogs, layered transition metal dichalcogenides (TMDs, list of abbreviations is presented in the Supplemental Information (**SI**)) have gained substantial interest over the last decades owing to their chemical versatility and exceptional physicochemical properties, including excellent mechanical properties, large specific surface areas, remarkable electronic performances, good chemical stabilities, high catalytic activities and facile synthesis processes, which all potentially benefit the development of high-performance biosensing applications (Kalantar-zadeh and Ou, 2015; Kenry and Lim, 2017; Thanh et al., 2018). The structure, composition, dimensionality and basic properties of layered TMDs are presented in Fig. S1 in the **SI**. Compared to graphene as the most studied two-dimensional (2D) candidate for biosensing, the tunable energy band gap (over the range of 0.2–2.1 eV) in TMDs in conjunction with their excellent optoelectronic properties make them suitable for the fabrication of ultrasensitive biosensors (Sarkar et al. 2014, 2015). This inspiring property of 2D TMDs will largely compensate for the weakness of gapless graphene, making them preferable candidates for the next-generation optoelectronic applications, especially biological sensing (Wang et al., 2017). More importantly, the cytotoxicity and genotoxicity of 2D TMDs are considered relatively low to most of the bio-species, which is the prerequisites for the application in biosensing (Chng and Pumera, 2015; Chng et al., 2014; Kaur et al., 2018). A comparison of the merits and disadvantage of 2D TMDs with those of graphene is presented in Table S1 in the **SI**. Nevertheless, the exploration of 2D TMDs for biosensing is still in its infant stage (Nirala et al., 2018). In this review article, the focus will be on the start-of-the-art contributions to the investigation of the 2D TMDs-based active materials as the key building units/components of various biosensors. The content mainly includes the synthesis of single- and few-layer TMDs, the manipulation of 2D TMDs, the fabrication of biosensors, and their detection performances towards a wide spectrum of bioanalytes and bio-species (e.g., DNA, proteins, and small biomolecules). Finally, our future perspectives will be presented for this subject that is undergoing an intense study.

* Corresponding author.
** Corresponding author.
E-mail addresses: huawenhu@126.com (H. Hu), cdcever@163.com (D. Chen), Jianzhen.ou@rmit.edu.au (J.Z. Ou).
[1] The authors contribute equally.

https://doi.org/10.1016/j.bios.2019.111573
Received 28 May 2019; Received in revised form 27 July 2019; Accepted 3 August 2019
Available online 07 August 2019
0956-5663/

Table 1
Summary of the key information on the reported 2D TMDs-based biosensors for the detection of diverse bioanalytes.

TMDs-based sensing platform	Preparation method	Analyte	LOD	Linear range	Comments	Ref.
MoS_2/graphene	CVD	DNA	1 aM	1 aM to 1 fM	i) graphene serves as a protection layer to prevent the reaction between MoS_2 and the ambient environment, and as a biocompatible interface layer to host DNA molecules on its surfaces ii) the PL intensity of the MoS_2 layer in the graphene/MoS_2 increases with the target ssDNA concentration	Loan et al. (2014)
MoS_2	mechanical exfoliation	pH, and streptavidin	i) 713 (for a pH change of 1 unit) ii) a sensitivity of 196 at 100 fM (for streptavidin)	3–9 (operation pH range)	semiconducting and atomically thin nature and the prowess of its 2D layered structure lead to excellent electrostatics and sensitivity	Sarkar et al. (2014)
MoS_2 (multilayer)	mechanical exfoliation	PSA	375 fM	NA	i)semiconducting nature with a direct bandgap ii)giant surface area for supporting a large number of probe molecules iii)2D nature enables low-noise operation iv)the change in the MoS_2 transistor drain current was caused by the specific binding of PSA to the antibodies that were immobilized onto the MoS_2 film surface	Wang et al. (2014a)
electrochemically reduced MoS_2 (1L)	Li-intercalation and then exfoliation	DA, and glucose	2 ppb	0–20 mM (for glucose); 1–50 μM (for DA)	good conductivity and unique 2D structure facilitate interactions with biomolecules	Wu et al. (2012)
MoS_2 (1L)	Li-intercalation and then exfoliation	DNA, and other biomolecules	500 pM	0–15 nM	high fluorescence quenching ability and different affinities to ssDNA and dsDNA	Zhu et al. (2013)
MoS_2, TiS_2, and TaS_2 (1L)	Li-intercalation and then exfoliation	DNA	0.05 nM (TaS_2), 0.1 nM (MoS_2), 0.2 nM (TiS_2)	0–5 nM (for all the TMDs-based biosensors)	high fluorescence quenching ability and different affinities to ssDNA and dsDNA	Zhang et al. (2015)
MoS_2/Au NPs	microwave-assisted hydrothermal	DA	80 nM	0.1–200 μM	i)increase in the electrocatalytic sites due to 2D MoS_2 defects ii)Au NPs increase the conductivity of the hybrid nanostructures	Su et al. (2013)
Au NPs-decorated PANI/MoS_2 composite	hydrothermal combined with an *in-situ* polymerization	DA	0.1 μM	1–500 μM	MoS_2 serves as a 2D conductive skeleton that can support a highly electrolytic accessible surface area of redox-active PANI and provided a direct path for electrons	Huang et al. (2014d)
HRP-modified MoS_2	ultrasonic-assisted direct liquid exfoliation	H_2O_2	0.26 μM	1–950 μM	the bioactivity of the immobilized HRP	Wang et al. (2013a)
HRP-TiO_2@WX_2 (X = S,Se,Te)	exfoliation of the lithium-intercalated WX_2 with *n*-BuLi and *t*-BuLi	H_2O_2	8.7 μm	0.5–30 μm, 50–300 μm, 500 μm-3 mM	i)faster electron transfer kinetics of TiO_2@ WX_2 (1T-phase) nanohybrid ii)enlarged surface area with an increased number of electrochemically active sites	Rahmanian et al. (2018)
Cu NPs functionalized MoS_2 NSs	liquid phase exfoliation of commercial MoS_2, and hydrothermal reaction	glucose	1055 mA mM^{-1} cm^{-2}	0–4 mM	i)Cu NPs show strong electrocatalytic activity toward glucose oxidation ii)the large specific surface area and active edges of MoS_2 contribute to the high sensitivity toward glucose oxidation	Huang et al. (2013a)
MoS_2/graphene (coupled with an enzyme, HRP)	hydrothermal	H_2O_2	0.049 μM	0.2 μM–1.103 mM	i)good biocompatibility and electron transport efficiency of the MoS_2/graphene composite ii)the high loading amount of HRP	Song et al. (2014)
WS_2	purchased reagent	glucose	2.9 μM	5–300 μM	peroxidase-like activity of WS_2.	Lin et al. (2014b)
MoS_2	purchased reagent (liquid phase exfoliation)	glucose	1.2 μM	5–150 μM	peroxidase-like activity of MoS_2.	Lin et al. (2014a)
MoS_2-aptamer probe	chemical exfoliation for the preparation of MoS_2	ATP, and α-thrombin	4 μM (for ATP); 300 pM (for thrombin)	10–2000 μM (for ATP)	fluorescence quenching performance of MoS_2.	Ge et al. (2014a)
MoS_2		streptavidin	0.67 ng mL^{-1}	0–600 ng mL^{-1}	fluorescence quenching performance of MoS_2	

(*continued on next page*)

Table 1 (*continued*)

TMDs-based sensing platform	Preparation method	Analyte	LOD	Linear range	Comments	Ref.
	exfoliation of the lithium-intercalated compound					Xiang et al. (2015)
WS_2	exfoliation of the lithium-intercalated MoS_2 (Li_xWS_2)	T4 PNK	0.01 U mL^{-1}	0.01–10 U mL^{-1}	fluorescence quenching performance of WS_2	Ge et al. (2014b)
WS_2	exfoliation of the lithium-intercalated MoS_2 (Li_xWS_2)	T4 PNK	0.05 U mL^{-1}	0.1–100 U mL^{-1}	fluorescence quenching performance of WS_2	Liu et al. (2014)
MoS_2/Au and Ag NPs	sonication-assisted liquid phase exfoliation of bulk MoS_2 and gradient centrifugation, followed by self-assembly of Au NPs	CEA	0.27 pg mL^{-1}	1 pg mL^{-1} to 50 ng mL^{-1}	i)through coupling with Au NPs, the formed Au NPs/MoS_2 shows enlarged specific surface area, enhanced conductivity, and promoted biocompatibility, as well as more efficiently immobilize the antibody ii)using Ag NPs-labeled Ab_2 as amplifying probes to further improve the sensitivity	Wang et al. (2015)
MoS_2	ultrasonication and gradient centrifugation	H_2O_2, glucose	2.5 nM (for H_2O_2), and 6.0 mM (for glucose)	5.0–100 nM (for H_2O_2); 2.0–16.0 mM (for glucose)	ultrasmall MoS_2 NPs with large surface area expose a large fraction of active edge sites	Wang et al. (2013b)
MoS_2/PANI	intercalation with self-doped PANI and ultrasonic exfoliation	adenine, guanine	6.3 nM	0.05–100 μM	negatively charged SPAN and MoS_2 and the strong π-π* stacking facilitate interactions with positive and rich-conjugated molecules	Yang et al. (2015c)
MoS_2/PXA	sonication-assisted liquid phase exfoliation, and electropolymerization	adenine and guanine	0.017 μM (for guanine) and 0.03 μM (for adenine)	0.5–10 μM (for both adenine and guanine)	PXA/MoS_2 nanocomposite owns the negative charge and specific structure, which obviously prompt the adsorption of the positively charged guanine and adenine	Yang et al. (2015b)
MoS_2/Pt NPs	microwave-assisted hydrothermal method	DA, and UA	0.17 (for DA) and 0.98 (UA) μM	0.5–150 and 5–1000 μM	synergistic effect of MoS_2 and Pt NPs	Chao et al. (2015a)
Au NPs coated-flowerlike VS_2/graphene	hydrothermal	nucleic acids or DNA (H5N1 gene sequence)	0.052 pM	0.0001–0.5 nm	i)VS_2 NFs provide a large surface area and good biocompatibility interface ii)graphene offers good conductivity iii)Au NPs not only serve as an immobilization matrix but also help to increase the conductivity of the composite film	Fang et al. (2015)
Au NPs-decorated $MoSe_2$ NFs	hydrothermal	OTA	0.08 pM	0.0001–1 nM	the large surface area of $MoSe_2$ NFs endowed them with a high capacity of loading aptamer and hence enhanced the sensitivity	Huang et al. (2016a)
Au NPs-decorated WS_2/AB	hydrothermal	hepatitis B virus genomic DNA	0.12 fM	0.001–100 pM	the good electrical conductivity, large specific surface area and WS_2/AB composite shows not only accelerated electron transfer but an increased amount of immobilized cDNA	Shuai et al. (2016)
WS_2/MWCNTs/Au NPs	hydrothermal	hepatitis B virus genomic DNA	2.5 fM	10 fM-0.1 nM	i)synergistic effect of WS_2/MWCNTs composite ii)HCR improves the sensitivity iii)improved electroactive area of electrode facilitates electron transfer	Liu et al. (2016)
$NiSe_2$	hydrothermal	glucose	23 nM	0.099–1252 μM	i)high electron transfer efficiency ii)a variety of complex differed in stoichiometry based on electronegativity difference between Ni (χ = 1.91) and Se (χ = 2.55)	Mani et al. (2017)
MoS_2/$NiCo_2O_4$	hydrothermal method and post-calcination	glucose	0.152 μM	1–1600 μM	the synergistic effects between petal-like MoS_2 NSs as a connector and hexagonal $NiCo_2O_4$ nanoplates as active sites	Wang et al. (2018)
MoS_2/Cu NFs	sonication-assisted liquid phase exfoliation for preparation of few-layer MoS_2, and electrodeposition of Cu NFs	H_2O_2 and glucose	0.021 μM (for H_2O_2) and 0.32 μM (for glucose)	0.04–1.88 μM and1.88–35.6 μM (for H_2O_2); 1–20 μM and 20–70 μM (for glucose)	i)the synergistic, catalytic effects of the Cu NFs and MoS_2 ii)the large surface area facilitates the adsorption of more target molecules	Lin et al. (2016)
MoS_2-Thionin	sonicating the mixture of MoS_2 and thionin in an ionic liquid and gradient centrifugation	DNA	0.19 μA mL ng^{-1} (sensitivity)	0.09 ng mL^{-1} to 1.9 ng mL^{-1}	i)electrochemical activity of thionin ii)MoS_2 sheets provide a good sensing platform for the immobilization of thionin	Wang et al. (2014b)

(*continued on next page*)

Table 1 (*continued*)

TMDs-based sensing platform	Preparation method	Analyte	LOD	Linear range	Comments	Ref.
					iii)interactions of dsDNA with thionin due to plenty of S edges on the MoS_2 sheets	
MoS_2/Au NPs	exfoliation of a Li-intercalated compound (MoS_2); microwave-assisted hydrothermal method (Au NPs-MoS_2)	glucose	2.8 μM	10–300 μM	the electron transfer of GOx at the electrode surface is boosted due to the Au NPs-MoS_2 modification	Su et al. (2014)
MoS_2 (NSs with small lateral dimensions, i.e., QDs)	Li intercalation of MoS_2 NPs followed by exfoliation	DNA	NA	NA	i)the small domain of the MoS_2 (lateral dimension of 10–20 nm) may cause the quantum confinement effect, leading to the enhanced band gap opening ii)MoS_2 NSs serve well as a quencher, but the quenching effect with an interval above 13 base pair seems insignificant	Feng et al. (2014)
MoS_2/Au NPs/Hb	(i) exfoliation of the *n*-BuLi-intercalated compounds (ii) microwave-assisted reduction reaction	H_2O_2	4 μM (for H_2O_2)	10–300 μM	excellent conductivity and biocompatibility of Au NPs@MoS_2 not only made the immobilized Hb keep its native biological activity but also facilitated the electron transfer between the electrode and the electroactive center of Hb	Chao et al. (2015b)
flowerlike MoS_2/Cu_2O	hydrothermal (MoS_2), and a precipitation process (Cu_2O/MoS_2)	glucose	1.0 μM	0.01–4.0 mM	high electrocatalytic activity of Cu_2O toward glucose oxidation, the large surface area of MoS_2 facilitated the immobilization of Cu_2O NPs, and fast heterogeneous electron transfer can be obtained on the interface between the Cu_2O and MoS_2	Fang et al. (2017)
$MoSe_2$/graphene	liquid exfoliation ($MoSe_2$), and solution-based sonication ($MoSe_2$/graphene)	NADH	1 μM	1–280 μM	i)the good conductivity of graphene ii)the presence of graphene can impede the aggregation of the $MoSe_2$, maximising the exposing of the active edges of $MoSe_2$	Selvarani et al. (2018)
MoS_2/Au-Pd	liquid-phase exfoliation and thermal coreduction	H_2O_2, glucose	0.16 μM (for H_2O_2) 0.40 μM (for glucose)	0.8 μM–10 mM (for H_2O_2) and 0.5–20 mM (for glucose)	i)high electrocatalytic activity of Au–Pd ii)synergy between Au–Pd bimetallic NPs and MoS_2 NSs	Li and Du (2017)
MoS_2/Fe_3O_4	sonication-assisted exfoliation	glucose	2.4 μM	5 − 150 μM	i)high peroxidase-like catalytic activities of Fe_3O_4 and MoS_2 ii)the Fe_3O_4 NPs work as stabilizers and allow the stable dispersion of MoS_2 in water	Nandwana et al. (2018)
MoS_2/SPAN	copolymerization (SPAN), and liquid exfoliation (MoS_2/SPAN)	CAP	0.065 μM	0.1–1000 μM	synergistic effect of MoS_2 NSs and SPAN on the reduction of CAP	Yang et al. (2015a)
MoS_2/Au-Pd-Pt	wet-chemistry method	H_2O_2	0.3 nM	1–100 nM	synergy between the highly dispersed trimetallic NF nanostructures and the MoS_2 NSs	Dou et al. (2018)
WS_2 (1T-phase)	exfoliation of lithium-intercalated WS_2	H_2O_2	2.0 nM	20 nM to 20 μM and 100 μM to 2 mM	desirable properties such as high surface-to-volume ratio, and excellent conductivity	Toh et al. (2017)
MoS_2	C_3N_4 sacrificial template-assisted thermolytic approach	glucose	~0.61 nM	8 nM-5 μM	i)3D porous framework of ultrathin MoS_2 NSs contributes to the adsorption of GOx and shortens the electronic diffuse distance ii)narrow band gap of MoS_2 NSs facilitates visible-light absorption	Wu et al. (2017)
MoS_2/Au NPs	exfoliation of Li-intercalated compound in water (MoS_2), and electrodeposition (MoS_2/Au NPs)	ATP, and thrombin	0.74 nM (for ATP) and 0.0012 nM (for thrombin)	1 nM to 10 mM (for ATP), 0.01 nM to 10 μM (for thrombin)	excellent conductivity of Au NPs, large surface area of MoS_2 NSs, and the synergy between MoS_2 and Au NPs	Su et al. (2016)
MoS_2/MWCNTs/Au NPs	L-cysteine-assisted solution-phase method	DNA	0.79 fM	10 fM to 10^7 fM	multicomponent synergies (MoS_2, MWCNT, and Au NPs) and multiple signal amplification	Huang et al. (2014b)
MoS_2, WS_2	Commercial product	DNA	LODs of ~3 nM for WS_2 and ~1.5 nM for MoS_2	NA	MoS_2 and WS_2 mainly rely on van der Waals force for the DNA adsorption, in contrast to GO involving π-π stacking and hydrogen bonding	Lu et al. (2017)
WS_2	commercial product	BLM and S1 nuclease	0.3 nM (for BLM), and 0.01 U mL^{-1} (for S1 nuclease)	0.5 nM–1000 nM (for BLM), and 0.05–2.5 U mL^{-1} (for S1 nuclease)	an irreversible scission of long ssDNA through the BLM-induced oxidation cleavage or S1 nuclease-induced enzymatic hydrolysis	Qin et al. (2015)

(*continued on next page*)

Table 1 (*continued*)

TMDs-based sensing platform	Preparation method	Analyte	LOD	Linear range	Comments	Ref.
MoS_2/graphene	liquid assisted exfoliation	Vi antigen	100 pg mL^{-1}	0.1 ng mL^{-1} to 1000 ng mL^{-1}	synergistic effect owing to easy biomolecular functionalization and enhanced conductivity	Pathania et al. (2018)
MoS_2 (few-layer)	CVD combined with e-beam evaporation	DNA	LOD of 10 fM, with a sensitivity of 17 mV/dec	a dynamic range of 10^6	hybridization of target ssDNA with the probe ssDNA physically adsorbed on the MoS_2 channel resulted in a shift of the threshold voltage in the negative direction and an increase in the drain current	Lee et al. (2015)
WS_2/B-PVA	a pulsed sonication-based exfoliation and functionalization	glycated hemoglobin (HbA1c)	33 nM	0–6 μM	the fluorescence of the B-PVA/WS_2 was quenched in the presence of HbA1c, whereas PVA/WS_2, not bearing boronic acid as a recognition moiety, showed no fluorescence changes upon the addition of the target	Yang et al. (2018)
assembly of water-soluble VS_2 QDs (with a lateral size of ~3.3 nm) and MnO_2 NSs	hydrothermal (VS_2 QDs) and solution reaction (VS_2 QDs/MnO_2 NSs)	glutathione	0.31 μM	0–500 μM	the fluorescence of VS_2 QDs can be significantly quenched by MnO_2 NSs due to FRET from VS_2 QDs to MnO_2 NSs, and the fluorescence recovery is realized by glutathione-enabled reduction of MnO_2 NSs	Du et al. (2018)
Ta_2NiS_5 and Ta_2NiSe_5	chemical vapor transport, and electrochemical Li-intercalation and exfoliation	DNA	50 pM	0–5 nM	high fluorescence quenching efficiency of single-layer Ta_2NiS_5 NSs	Tan et al. (2015)
WSe_2 (p-type)	mechanical exfoliation	DNA	50 nM	NA	the Cy3 dye attached p-DNA causes the fluorescence quenching of WSe_2 monolayer and redshift of the emission peak, while the addition of t-DNA partially recovers the quenched fluorescence	Han et al. (2017)
MoS_2 QDs (water-soluble)	hydrothermal	HAase	0.7 U mL^{-1}	1–50 U mL^{-1}	first quenching of the fluorescence by HA-functionalized Au NPs through a PIET mechanism, and subsequent fluorescence recovery via cleaving HA with HAase, aggregating Au NPs and blocking the PIET effect	Gu et al. (2016)
MoS_2	sonication-assisted liquid exfoliation	*E. coli*	94 CFU/mL	1000–8000 CFU/mL	i)higher optical absorption efficiency, thermal stability and strong binding sites for antibody immobilization	Kaushik et al. (2018)
MoS_2-deposited Au coated fiber optic SPR sensor	electro-dissolution	BSA protein	0.29 μg/mL	10–50 μg/mL	i)MoS_2 provides with more hydrophobic surface with more antibodies binding sites ii)synergy between MoS_2 and gold metallic thin film	Kaushik et al. (2019)
WS_2, MoS_2, WSe_2, and $MoSe_2$	kitchen blender-assisted shear exfoliation	DNA	1.54 nM (by ssDNA hybridization), 0.23 nM (by HCR)	2.0–20 nM (by ssDNA hybridization), 0.5–7.5 nM (by HCR)	i)metal ion-induced aggregation behavior ii)discriminative affinity of TMD NSs towards ssDNA and dsDNA iii)HCR is introduced to further enhance the sensitivity	Lan et al. (2019)
WS_2 NSs/Ag NCs	sonication-assisted exfoliation; in situ reduction of Ag^+	H_2O_2, glucose	fluorescence: 0.26 nM (for H_2O_2), 21 nM (for glucose); colorimetric: 0.72 μM (for glucose)	0.01–2 μM (for H_2O_2), 0.05–400 μM (for glucose)	i)difference in the Fermi energy levels of Ag NCs and WS_2 NSs, facilitating charge separation ii)the peroxidase mimetic activity of the WS_2 NSs/Ag NCs nanocomposite	Khataee et al. (2018)
MoS_2	L-cysteine-assisted solution-phase method	choline	0.4 μM	1–160 μM	i)enzyme mimetic catalytic activity of MoS_2 NSs in catalyzing the oxidation of TMB in the presence of H_2O_2 ii)p-type nature of MoS_2 NSs facilitates the charge transfer from TMB to MoS_2 NSs.	Nirala et al. (2018)
1L WS_2/PFVCN	commercial product	S1 nuclease	5×10^{-6} U/mL	NA	fluorescence quenching of PFVCN by 1L WS_2 after hydrolysis of ssDNA-PFVCN complex by S1 nuclease	Li et al. (2016)
WS_2-Co^{2+}/ABEI-Au	commercial product (WS_2)	*S. aureus*	15 cfu/mL	50 to 1.5×10^5 cfu/mL	chemiluminescence quenching by WS_2 NSs	Hao et al. (2017b)
WS_2/graphene/Au	modified L-cysteine-assisted solution-phase method	DNA	0.0023 pM	0.01–500 pM	i)highly electrolytic accessible surface area of WS_2	Huang et al. (2014a)

(*continued on next page*)

Table 1 (*continued*)

TMDs-based sensing platform	Preparation method	Analyte	LOD	Linear range	Comments	Ref.
					ii)dual signal amplification in the WS_2/graphene/Au NPs composites-modified GCE with good charge transport and large surface area	
WS_2	commercial product	microRNAs	~180 pM	0.5–10 nM	the CRET process between the chemiluminescent donor (luminol) and chemiluminescent acceptor (WS_2 NSs)	Zhao et al. (2015)
$MoSe_2$/graphene	hydrothermal	PDGF-BB	20 fM	0.0001–1 nM	i)ultrathin 2D planar structures, high surface areas, good electrical conductivity and superior electrochemical performance of MoS_2-graphene composites ii)high specificity of aptasensor iii)Exo III-aided signal amplification	Huang et al. (2016b)
MoS_2, $MoSe_2$, WS_2, WSe_2 (1T-phase)	exfoliation of *t*-BuLi-intercalated compounds	fenitrothion	2.86 nM	1–1000 nM	i)metal-like nature of 1T-phase TMDs in enhancing sensitivity for analytical detection ii)high specificity of acetylcholinesterase iii)inhibition effect of fenitrothion on acetylcholinesterase	Nasir et al. (2017)

Note: [a]Sensitivity (defined as the ratio of the difference in the current before and after biomolecule binding to the lower of the two currents) as high as 196 was achieved in the subthreshold region for a 100 fM streptavidin solution.
NA: not available from the corresponding literature.

2. Cytotoxicity and genotoxicity of 2D TMDs

The cytotoxicity of 2D TMDs has early been explored; for example, the cytotoxicity of three common exfoliated TMDs, including MoS_2, WS_2, and WSe_2, was probed by cell viability assessments, along with a comparison with those of graphene oxide (GO) and halogenated graphene (HG). MoS_2 and WS_2 nanosheets (NSs) induced considerably low cytotoxicity to A549 cells and were much less hazardous in comparison with GO and HG. By contrast, WSe_2 showed higher cytotoxicity, similar to GO and HG, which might be correlated with the identity of the chalcogen (Teo et al., 2014). Additionally, the toxicity of exfoliated MoS_2 was found to rely on the exfoliation degree that could be tuned through interactions with different intercalation agents (Chng et al., 2014); stronger cytotoxicity was observed for the MoS_2 with the higher degree of exfoliation, likely originating from the increased surface area and active edge sites. In a review article on the toxicity of 2D TMDs and graphene-related materials, the toxicity of 2D TMDs was also found to depend on the fabrication methods and was shown to be lower than that of GO (Chng and Pumera, 2015). To further promote their biocompatibility for *in vivo* biomedical applications, graphene materials (Sun et al., 2008) and exfoliated TMDs (Hao et al., 2017a) were usually pre-functionalized by polyethylene glycol (PEG). It was demonstrated that three kinds of PEG-functionalized TMDs (including MoS_2, WS_2, and TiS_2) showed no significant *in vitro* cytotoxicity, while PEG-MoS_2 exhibited much smaller *in vivo* cytotoxicity in comparison with PEG-WS_2 and PEG-TiS_2 because PEG-MoS_2 could be biodegraded and quickly excreted almost completely from the organs (Hao et al., 2017a). In addition to cytotoxicity tests, genotoxicity examination was also conducted on 2D MS_2 (M = Mo, W), and low cytotoxicity and genotoxicity were demonstrated in both mechanically exfoliated MS_2 and CVD-grown MS_2 (Appel et al., 2016). More information regarding the biocompatibility and nanotoxicity of 2D layered materials can be referred to a recent review article (Kenry and Lim, 2017).

3. Fabrication of single- and few-layer TMDs for biological sensing applications

A large number of methods have been used to prepare single- or few-layer TMD NSs, which have their own advantages and disadvantages, as summarized in Table S2 in the **SI**. The synthetic methods should be oriented to the specific application of 2D TMDs. In the **SI,** solid-, liquid-, and vapor-phase synthetic approaches are discussed in detail by category (Figs. S2 and S3). From Table 1, it can also be noted that gas-phase approaches (especially CVD) are suitable to fabricate FETs-based biosensors relative to most of solid- and liquid-phase methods since single-layer (1L) TMDs can be directly grown on a substrate, as the active channel material of FETs-based biosensing devices. Some solid-phase methods such as mechanical exfoliation have also been adopted for the fabrication of FETs-based biosensing devices because the mechanically exfoliated TMD NSs can be easily transferred to a substrate (e.g., Si/SiO_2) to work as the channel material of the device. Due to their cost-effective, facile and up-scalable characteristics, liquid-phase methods are the most intensively investigated ones for various optical and electrical biosensing applications, as evidenced by the summary in Table 1, e.g., the liquid-phase exfoliation methods are frequently employed to fabricate 2D TMDs for the modification of glassy carbon electrode (GCE) for electrochemical biosensing applications.

4. Biosensing applications

The wide use of 2D TMDs in the biological sensing field is due to their many advantages which render them highly promising for the construction of various sensing platforms to achieve extremely sensitive detection. For example, 2D TMDs possess larger accessible surface area as compared to those with other types of structures such as

nanoparticles (NPs), nanotubes, nanocubes, and nanorods. The 2D configuration can also impart the largest interfacial contact area between 2D TMDs and electrodes, facilitating the strongest interfacial interactions and hence rapid interfacial charge transfer and robust biosensing performance. In addition, the larger specific surface area of 2D TMDs allows for immobilizing more signal or receptor molecules onto the modified electrode surface and for enhanced mass transport. Some of 2D TMDs (such as metallic 1T-WS_2) also possess good electronic conductivity which facilitates the charge transfer to the electrodes. The unique catalytic properties of 2D TMDs contribute to signal amplification and stimulate the translation of biorecognition events to a fast optical, colorimetric, or electrochemical response (Liu et al., 2016). TMD NSs can be easily modified by foreign species to impart enhanced functions for versatile sensing applications. Particularly, unique bonding between metal and sulfur atoms can readily form when metallic species are considered as the modifier for MS_2 (M = Mo, W Ti, Zr, Hf, V, Nb, Ta, Tc, Re) (Huang et al., 2016a; Wang et al., 2015), a characteristic that is lacking in many other kinds of nanomaterials such as graphene, carbon nanotubes (CNTs) and transition metal oxides. The modification/functionalization can effectively convert the semiconducting TMD NSs to conducting TMDs-based nanocomposites, and synergies normally exist in the multiple compositions.

Table 1 summarizes of the state-of-the-art contributions made in this current and broad topic area of using 2D TMDs to construct various sensing systems for the detection of various bioanalytes, such as proteins, DNA, and small biomolecules.

4.1. Optical platform

4.1.1. Fluorescence and chemiluminescence (CL)-based

4.1.1.1. Fluorophore-labeled, TMDs-based biosensing platform. Based on the intrinsic fluorescence quenching properties of 2D TMDs through possible fluorescence resonance energy (or electron) transfer (FRET), many sensing platforms have been fabricated on the basis of various FRET pairs (e.g., a fluorophore-2D MoS_2 pair), especially for dye-labeled DNA as the probe. Considering that the rigid double-stranded DNA (dsDNA) has much weaker adsorption interactions with 2D TMDs as compared to the single-stranded DNA (ssDNA), the controllable switching of ssDNA to dsDNA makes the fluorescence “turn on”, and vice versa. The strong adsorption interaction between ssDNA and TMD NSs is achieved by the van der Waals force between nucleobases and the basal plane of TMD NSs (Ge et al., 2014a; Zhu et al., 2013), while after the hybridization of ssDNA with the target and hence the formation of dsDNA, the nucleobases become buried between the negatively charged helical phosphate backbones in a high density, largely weakening the interactions between the formed dsDNA and TMD NSs. Zhang group presented the first demonstration that 1L MS_2 (M = Mo, Ti, Ta) possessed high fluorescence quenching efficiency and different affinities toward ssDNA and dsDNA (Zhang et al., 2015; Zhu et al., 2013), and realized the sensitive and selective detection of DNA and adenosine with a fluorescent dye-labeled aptamer as the probe and 1L MoS_2 as the substrate (Fig. 1a). Thereafter, Yu group reported different DNA-TMDs NSs sensing platforms for the detection of proteins using MoS_2 NSs as the substrate and a fluorescent dye-labeled DNA aptamer as the probe (Ge et al. 2014a, 2014b; Liu et al., 2014). The fluorescence of the dye-labeled DNA aptamer was initially quenched by MoS_2 NSs, and hybridization with the complementary target molecules could release the aptamer-probe away from MoS_2, resulting in fluorescence retention (Fig. 1b) (Ge et al., 2014a). Later, Yu group investigated a 2D WS_2 sensing platform for the analysis of T4 polynucleotide kinase (T4 PNK) and T4 PNK phosphatase (T4 PNKP), as shown in Fig. 1c and d, respectively (Ge et al., 2014b; Liu et al., 2014). Two kinds of probes were designed based on DNA phosphorylation (Ge et al., 2014b) and dephosphorylation of the 3′ termini of nucleic acids (Liu et al., 2014). In the presence of T4 PNK, a fluorescent dye-labeled dsDNA could be phosphorylated and then specifically degraded by λ-exonuclease, yielding ssDNA that had strong interactions with 2D WS_2 and hence quenching the fluorescence (Fig. 1c). By contrast, without T4 PNK-catalyzed phosphorylation, the λ-exonuclease-induced degradation of dsDNA was prohibited. For the T4 PNKP detection, it could hydrolyze the phosphorylated ssDNA probe into the ssDNA with a 3′-hydroxyl end, which was immediately elongated to form dsDNA by Klenow fragment polymerase (Fig. 1d). More recently, Huang group designed a MoS_2-based sensing platform for the streptavidin detection through a combined process of terminal protection of small-molecule-linked DNA (TPSMLD) and exonuclease III (Exo III)-aided DNA recycling amplification (Xiang et al., 2015). In the TPSMLD process (Fig. 1e), streptavidin could specifically bind with biotin being linked to probe 1, avoiding the enzymolysis of probe 1 by exonuclease I (Exo I). The survived probe 1 could subsequently hybridize with probe 2 to release probe 2 from the MoS_2 surface, thus partially recovering the fluorescence. Nevertheless, the single TPSMLD process was still unsatisfactory to achieve the sensitive streptavidin detection. To address this, Exo III-aided DNA recycling amplification was further introduced into the TPSMLD process (Fig. 1f). In the presence of streptavidin that could specifically bind biotin, probe 1 was protected from the Exo I-catalyzed digestion. Upon incubation with Exo III and the probe 2-MoS_2 complex, the probes 1 and 2 were hybridized, accompanied by the gradual degradation of probe 2 from 3′-to-5′-end by Exo III. As a result, the remaining probe 1 could be repeatedly involved in new cycles of hybridization with probe 2, releasing more fluorescent dye-labeled probe 2 from the MoS_2 surface and hence yielding stronger fluorescence. The sensing performances of MS_2 NSs (M = Mo,W) toward DNA were also compared with that of their analog (i.e., GO). It was consistently demonstrated that DNA was adsorbed onto MS_2 NSs (M = Mo,W) mainly via van der Waals force as compared to GO via π-π stacking and hydrogen bonding, and a less fluctuated background signal was observed for these 2D TMDs-based biosensor (Lu et al., 2017).

When TMD NSs are manufactured into TMD quantum dots (QDs), exotic PL properties would be generated due to the quantum confinement effect. Additionally, through intentionally creating nano-scale point defects in the hexagonal lattice of pristine 1L MS_2 (M = W, Mo), the PL properties were significantly affected (Chow et al., 2015). The optical properties of TMDs NSs can thus be tailored by size manipulation and defect creation for optoelectronic applications. Taking 10–20 nm-sized MoS_2 QDs as an example, they exhibited an inherent blue PL at 415 nm under 300 nm UV illumination (Feng et al., 2014). A FRET pair was subsequently constructed by attaching the Alexa 430-labeled dsDNA with poly G tails onto the MoS_2 QDs, and systematic FRET studies on the Alexa 430-dsDNA-MoS_2 conjugates were conducted for the investigation of the acceptor and donor capability of the MoS_2 QDs (Feng et al., 2014). While ssDNA was attached to the MoS_2 surface via van der Waals force (Vovusha and Sanyal, 2015), the hybridization of ssDNA would lead to the formation and separation of the dsDNA from the MoS_2 basal plane. Therefore, the dual roles of blue-luminescent MoS_2 QDs in the FRET phenomenon were demonstrated.

4.1.1.2. Label-free, TMDs-based biosensing platform. Considering that fluorophore labeling is complex, high-cost, and time-consuming, label-free strategies on the basis of various sensing platforms are more desirable for practical applications (Hu et al., 2014; Lee et al., 2015; Li et al., 2015; Sarkar et al., 2014; Wang et al., 2014a; Yadav et al., 2019). The label-free fluorescence-based detection of S1 nuclease was achieved on 2D WS_2 using a fluorescent conjugated polymer as the signal reporter (Li et al., 2016). This polymer firstly formed a complex with ssDNA. Its fluorescence could be quenched by the 2D WS_2 after the hydrolysis of ssDNA in the complex into fragments by S1 nuclease and the subsequent adsorption of the polymer onto the 2D WS_2. The CLresonance energy transfer (CRET) between the donor and acceptor (2D TMDs) was also explored for the label-free detection of

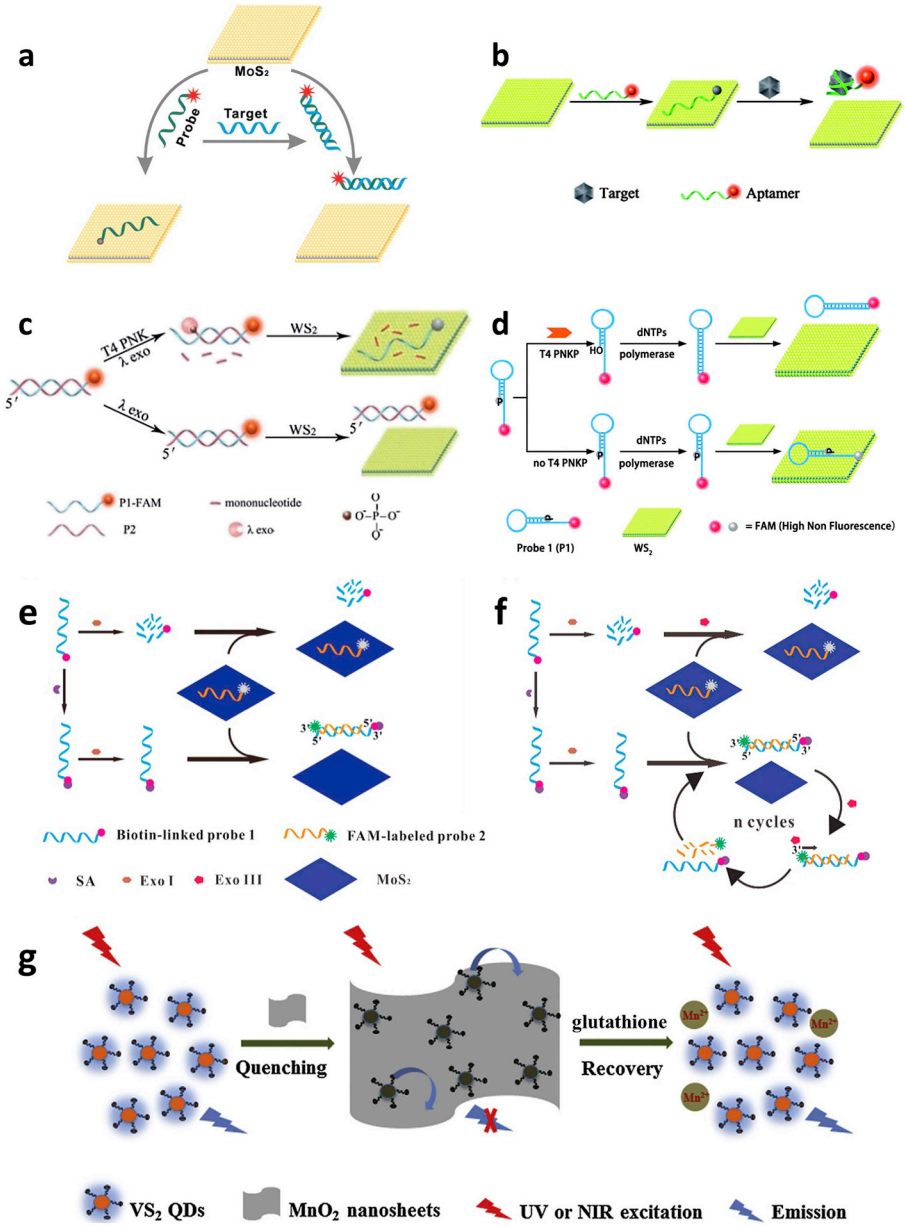

Fig. 1. a) Scheme of a fluorimetric DNA assay using 2D MoS_2 as the sensing platform. Reproduced with permission from (Zhu et al., 2013). Copyright 2013, American Chemical Society. b) Scheme of a 2D MoS_2-based effective sensing system. Reproduced with permission from (Ge et al., 2014a). Copyright 2014, Royal Society of Chemistry. c) Scheme of the WS_2 NS-based sensing platform for the detection of the T4 PNK activity and for the inhibition analysis. Reproduced with permission from (Ge et al., 2014b). Copyright 2014, Royal Society of Chemistry. d) Scheme of a 2D WS_2-based platform for sensing the T4 PNKP activity and for analyzing the inhibition. Reproduced with permission from (Liu et al., 2014). Copyright 2014, Royal Society of Chemistry. e,f) Illustration of the mechanism of a 2D MoS_2-based biosensor for the detection of streptavidin via a combined process of the TPSLMD (e) and Exo III-aided DNA recycling amplification (f). Reproduced with permission from (Xiang et al., 2015). Copyright 2015, Elsevier. g) Scheme of VS_2 QDs/MnO_2 NSs sensing platform for monitoring glutathione. Adapted with permission from (Du et al., 2018). Copyright 2018, Elsevier.

biomolecules, such as microRNA (Zhao et al., 2015). Besides the above fluorescence and CL as generated from the other species than 2D TMDs, the exploitation of the autofluorescence of TMD QDs is also considered as an effective way for the label-free detection of bioanalytes by both "turn on" and "turn off" the fluorescence in a qualitative manner (Du et al., 2018; Fahimi-Kashani et al., 2017). Most recently, water-soluble VS_2 QDs were synthesized as an autofluorescent platform, and the fluorescence could be heavily quenched by MnO_2 NSs. The addition of glutathione turned on the quenched fluorescence of the VS_2 QDs/MnO_2 NSs assembly by reducing MnO_2 NSs into Mn^{2+}, realizing the label-free detection of glutathione, as shown in Fig. 1g (Du et al., 2018). This study also investigated the optical fluorescence biosensor under NIR excitation which notably reduced the background signals and also avoided damage to biological tissues as normally caused by UV irradiation.

4.1.2. Absorption-based

Compared to graphene with zero bandgap energy, layered TMDs, with semiconductive properties, exhibit characteristic visible absorption, which can thus be exploited for the absorption-based biosensing through inducing a regular change of their visible absorption. This optical biosensing is low-cost, simple, and highly sensitive. For example, a water dispersion of MoS_2 NSs exhibited a rapid aggregation response to salts due to a salt-induced effect (Li et al., 2015), and, reversely, a homogeneous dispersion was exhibited even in the presence of high-concentration salts when the 2D MoS_2 surface was protected by a ssDNA layer. The replacement of ssDNA with dsDNA made a loss of the protective effect, and severe aggregation started. The label-free detection was thus achieved by virtue of this discrimination capability to ssDNA and dsDNA, as well as the size-dependent optical absorption of MoS_2 NSs (Fig. 2a). Apart from the ssDNA hybridization strategy in the optical biosensor based on the salt-induced aggregation of TMD NSs, a hybridization chain reaction (HCR) was introduced to further enhance the DNA detection sensitivity, and the LOD was lowered from 1.54 nM by ssDNA hybridization to 0.23 nM by HCR (Lan et al., 2019).

4.1.3. Colorimetric

Due to no requirement on any sophisticated instrumentation, colorimetric methods show great potential for portable and scalable applications. The enzyme-mimetic inorganic nanomaterials have featured

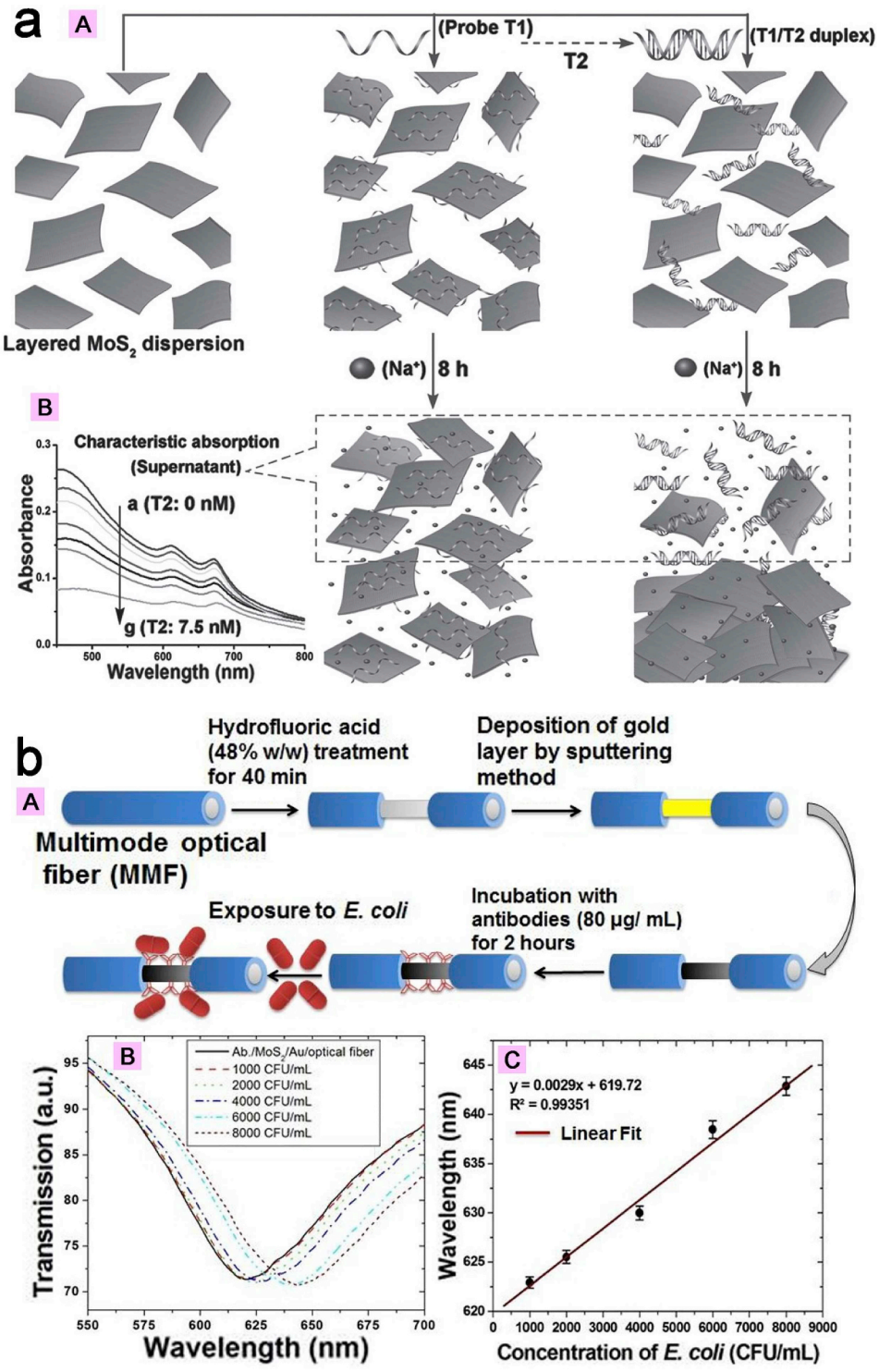

Fig. 2. a) Scheme of a label-free DNA biosensor constructed based on the ssDNA-induced dispersion of layered MoS_2 in an aqueous salt solution (A), and the absorption spectra of layered MoS_2 in the presence of different amounts of the complementary target ssDNA, T2 (from 0 to 7.5 nM) with the fixed concentration of the probe ssDNA, T1 (7.5 nM) (B). Reproduced with permission from (Li et al., 2015). Copyright 2015, Wiley-VCH Verlag GmbH & Co. b) Scheme of the procedures for the development of an SPR immunosensor with MoS_2 NSs as the interfacing layer for effective biofunctionalization (A), transmission spectra of the Ab/MoS_2/Au/optical fiber immunosensor, depicting resonance wavelengths corresponding to the different concentration of *E. coli* (B), and dependence of the resonance wavelength on the *E. coli* concentration for the prepared immunosensor (C). Reproduced with permission from (Kaushik et al., 2018). Copyright 2018, Elsevier.

as an emerging class of ideal tools for colorimetric detection due to their controllable structure and composition, high stability, easy preparation, and tunable catalytic activity (Lin et al., 2014a). Enzyme mimetics possess many advantages over natural enzymes, such as lower cost, and greater stability against denaturing or protease digestion. For example, pristine MoS_2 NSs were evidenced with enzyme mimetic catalytic activity for the oxidation of 3,3′,5,5′-tetramethylbenzidine (TMB) in the presence of H_2O_2, which was exploited to detect choline based on the reaction of choline and choline oxidase to produce H_2O_2. Dip test strips were also fabricated using filter paper as a flexible and visual platform that was pretreated with a mixture of TMB and MoS_2 NSs. The pretreated dip test strips were then used for the choline detection in real samples including milk and serum which were pre-mixed with choline oxidase to yield H_2O_2 (Nirala et al., 2018). In addition, a Fe_3O_4/MoS_2 0D/2D nanocomposite was demonstrated with a peroxidase-like activity for the non-enzymatic detection of glucose (Nandwana et al., 2018). The Fe_3O_4 NPs (anchored on the MoS_2 NSs) contributed to the formation of a stable aqueous dispersion of the Fe_3O_4/MoS_2 nanocomposite, facilitating its sensing applications with easy operation. Noninvasive point-of-care glucose diagnostics were also achieved in this study by means of the inkjet printing of Fe_3O_4/MoS_2 nanocomposites together with other active sensing elements onto

paper, producing test strips for the qualitative and quantitative colorimetric detection of glucose at a concentration down to 2.4 μM (Nandwana et al., 2018). However, the colorimetric strategies were demonstrated with a smaller sensitivity compared to other detection methods such as fluorescence, and the former resulted in a much higher LOD value (0.72 μM) for the glucose detection than the latter (21 nM) (Khataee et al., 2018).

4.1.4. Plasmonic-based and surface-enhanced Raman spectroscopy (SERS)-based

When TMD layers are deposited on metallic thin films or functionalized with metallic NPs (e.g., Au or Ag), the strong coupling can be induced at the metal/TMD interface due to the effective charge transfer, and a large electric field enhancement at the interface can be generated. As an evanescent wave, the electric field excited on the metallic surface is sensitive toward the refractive-index change of its surrounding media. This phenomenon is generally referred to as surface plasmon resonance (SPR). SPR-based optical biosensors are commonly used for the real-time monitoring of various biomolecular interactions such as DNA hybridization and protein binding. By virtue of their high optical absorption efficiency and unique electronic structure, 2D TMDs have been widely used for constructing SPR biosensing platforms. For example, a configuration of an SPR biosensor was theoretically proposed using a MoS_2-graphene hybrid, which exhibited a more than 500-fold larger phase-sensitivity enhancement factor when compared to the SPR sensing scheme without the hybrid coating or with only graphene coating (Zeng et al., 2015). While graphene acted as a bio-recognition component for capturing the target biomolecules through π-stacking force, MoS_2 layers were used to improve light absorption so as to provide enough excitation energy for efficient charge transfer. The theoretical analysis showed that electron transfer as generated by the work functions difference among graphene, MoS_2, and Au would result in a large electric field enhancement at the sensing interface and consequently a high sensitivity. In addition to improving light absorption, MoS_2 was also reported as a bio-recognition layer in a metal/graphene/MoS_2 configuration of an SPR-based fiber optic biosensor (Mishra et al., 2016). To increase the quality factor and detection accuracy, a silicon layer was also included between metal and MoS_2 layers in a graphene/MoS_2 hybrid-based SPR biosensor (Maurya et al., 2015). Furthermore, silicon NSs were employed to combine with 2D TMDs (including MoS_2, $MoSe_2$, WS_2, and WSe_2) for enhancing the sensitivity of an SPR biosensor (Ouyang et al., 2016). Most recently, MoS_2 NSs-functionalized fiber optic SPR biosensors were also investigated to detect *E. coli* (Kaushik et al., 2018), as shown in Fig. 2b, and bovine serum albumin (BSA) (Kaushik et al., 2019).

4.2. Electrical platform

4.2.1. Electrochemical-based

The electrochemical detection involves redox reactions of bioanalytes at the electrode-electrolyte interface, generating the bioanalyte concentration-dependent redox current (Selvarani et al., 2018; Shuai et al., 2016). Electrochemical techniques possess many advantages for biosensing, including high sensitivity, facile operation, low cost, reusability, prompt response, trace sampling, and fast analysis (Lin et al., 2016; Liu et al., 2016; Mani et al., 2017; Wang et al. 2014b, 2018). A portable and universal biosensing platform can also be fabricated via electrochemistry. As a result, electrochemical biosensors have gained particular interest over these years (Shuai et al., 2016).

Electrochemical test strongly relies on electrodes, and bare electrodes (e.g., GCE) suffer from high over-potential and low sensing signal (Wang et al., 2018). To promote the detection signal, the GCE surface modification is necessary. In this respect, rationally designed 2D TMDs and their nanocomposites have been widely applied as the modifier for electrochemical sensing in both the enzymatic and non-enzymatic manner. Because most of TMDs are semiconductors and lack direct path for electrons (Bollella et al., 2017), relatively little attention has been paid to using neat TMD NSs as the modifier to construct electrochemical sensing platforms. Nevertheless, modulation of their internal structure might be effective for the production of neat 2D TMDs with high electrocatalytic activity. Recently, Pumera group systematically exfoliated the tert-butyllithium (*t*-BuLi)-intercalated TMDs including MoS_2, $MoSe_2$, WS_2, and WSe_2 as the biosensing platform for the fenitrothion detection (Nasir et al., 2017). The prepared samples existed predominantly in the metallic 1T-polymorph (with metal-like property), a structure favorable for enhancing the sensitivity. The sensing mechanism was mainly based on the inhibition of fenitrothion to enzyme activity and hence the significant weakening of the electrochemical signal of the redox reaction catalyzed by the 1T-phase TMDs. It was also demonstrated that 1T-phase WS_2 outperformed all the other 2D TMDs. The illustration of the construction of the biosensor using 1T-phase TMD NSs as the platform is shown in Fig. 3a.

Due to the limited space for enhancing the sensitivity of the neat TMDs, researchers are motivated to incorporate various electrically conducting components onto TMDs for producing the TMDs-based nanocomposites, such as graphene, CNTs, conducting polymers, and noble metal NPs (Huang et al. 2014b, 2014d; Yang et al., 2015a). For example, a promoted electrical transport pathway and enhanced stability were achieved through anchoring MoS_2 NSs to a support with a robust conductivity (Wang et al., 2018).

4.2.1.1. Metal NPs as the modifier. Usually, the incorporation of noble metal NPs helps to realize a direct electron transfer between the electrode and the enzyme (e.g., horseradish peroxidase (HRP) being specific to H_2O_2) in a TMD NSs-based biosensor (Bollella et al., 2017). By contrast, there would be a large distance between the active site of HPR and the electrode in the absence of the metal NPs since the active center of the HPR is deeply embedded in the protein shell, and such a distance is too large to realize an efficient electron transfer (Bollella et al., 2017). The incorporation of noble metal NPs enables a large decrease in the distance between the active site and the microelectrodes and can also lower the overpotential of H_2O_2, thereby avoiding the fouling of the electrode as caused by the co-deposition of HRP-metal NPs (Bollella et al., 2017).

Au NPs are most frequently employed to modify semiconducting TMDs NSs (Huang et al. 2014c, 2014d; Su et al. 2013, 2014; Wang et al., 2015). As shown in Fig. 3b, a homogeneous dispersion of MoS_2 NSs and Au NPs, together with glucose oxidase (GOx), were cast onto GCE, yielding a modified electrode for the electrochemical detection of glucose based on Equation (1) (Su et al., 2014). The incorporation of Au NPs onto the MoS_2 NSs promoted the electron transfer between the GOx and electrode and hence enhanced the sensitivity, as evidenced by a cyclic voltammetry (CV) study.

$$\text{Glucose} + O_2 \xrightarrow{\text{GOx}} \text{Gluconolactone} + H_2O_2 \quad (1)$$

To amply the detection signal for an electrochemical biosensor, an additional Ag nanospheres-GOx probe was further introduced into the MoS_2@Au NPs sensing system for the detection of carcinoembryonic antigen (CEA) based on Equations (2)–(5) (Wang et al., 2015), as schematically presented in Fig. 3c. Due to specific antigen-antibody complexing, a larger CEA concentration would lead to a higher amount of Ag nanospheres-GOx. In the presence of glucose, the more GOx that was accessible for catalyzing the glucose oxidation under aerobic conditions could produce more H_2O_2. The further catalytic reduction of plenty of H_2O_2 over Au NPs@MoS_2 strongly reduced the current exhibited by the differential pulse voltammetry (DPV) curves.

$$\text{Glucose} + O_2 \xrightarrow{\text{GOx}} \text{Gluconic acid} + H_2O_2 \quad (2)$$

$$H_2O_2 + MoS_2 \rightarrow HO + MoS_2OH \quad (3)$$

$$H_2O_2 + HO \rightarrow HOO + H_2O \quad (4)$$

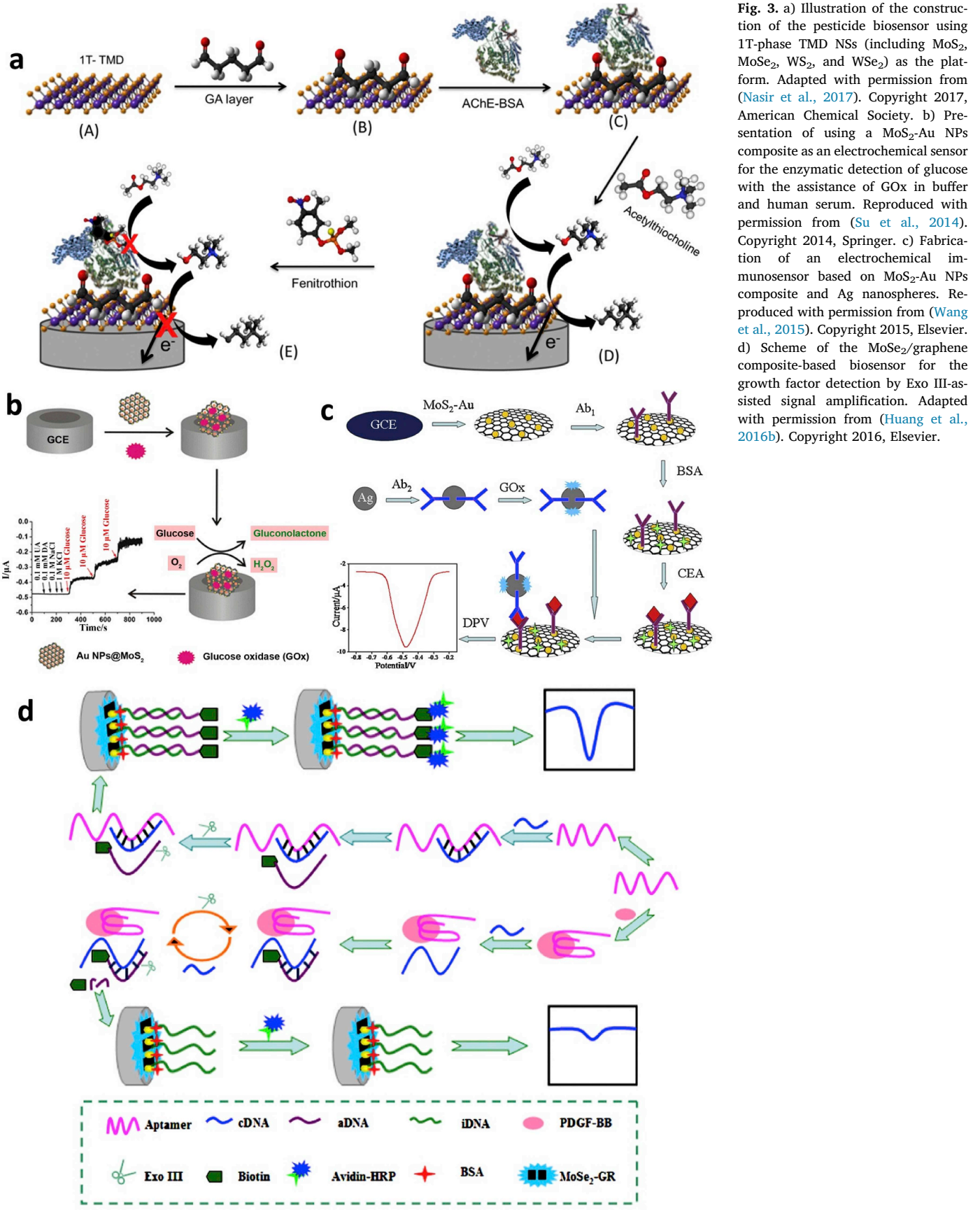

Fig. 3. a) Illustration of the construction of the pesticide biosensor using 1T-phase TMD NSs (including MoS_2, $MoSe_2$, WS_2, and WSe_2) as the platform. Adapted with permission from (Nasir et al., 2017). Copyright 2017, American Chemical Society. b) Presentation of using a MoS_2-Au NPs composite as an electrochemical sensor for the enzymatic detection of glucose with the assistance of GOx in buffer and human serum. Reproduced with permission from (Su et al., 2014). Copyright 2014, Springer. c) Fabrication of an electrochemical immunosensor based on MoS_2-Au NPs composite and Ag nanospheres. Reproduced with permission from (Wang et al., 2015). Copyright 2015, Elsevier. d) Scheme of the $MoSe_2$/graphene composite-based biosensor for the growth factor detection by Exo III-assisted signal amplification. Adapted with permission from (Huang et al., 2016b). Copyright 2016, Elsevier.

$$MoS_2OH + HOO \rightarrow H_2O + O_2 + MoS_2 \quad (5)$$

In situ electrochemical monitoring of H_2O_2 secreted by live cancer cells was also performed using a trimetallic nanoflower nanostructures-modified MoS_2 NSs (Dou et al., 2018), and the combination of different metallic elements endowed the composite sensor with enhanced catalytic performance as compared to the single-phase counterparts. A highly branched or dispersed nanostructure such as nanoflower (Dou et al., 2018) and dendrite (Naveen et al., 2016) of bimetallic and trimetallic NPs was useful for obtaining a high catalytic activity, contributing to an impressive sensitivity of the trimetallic nanoflower-modified MoS_2 (linear range: 1–100 nM; LOD: 0.3 nM) (Dou et al., 2018).

4.2.1.2. Carbon nanomaterials as the modifier. Carbon nanomaterials are also popular choices for the modification of TMDs NSs due to their superior electronic conductivities, excellent mechanical strength, and high chemical stability. The synergies between TMD NSs and carbon nanomaterials are highly expected to dramatically enhance the electrocatalytic activity and stability. For instance, a MoS_2/graphene hybrid was reported to modify GCE for the enzymatic detection of H_2O_2 using HRP as the enzyme (Song et al., 2014). A $MoSe_2$/graphene composite was also investigated as the sensing platform of an electrochemical aptasensor for the enzymatic detection of platelet-derived growth factor BB (PDGF-BB), as shown in Fig. 3d. While the sensing platform provided with large surface area, good electrical conductivity and superior electrochemical performance, the high specificity and stability of the aptasensor combined with Exo III-assisted signal amplification contributed to the high performance in the PDGF-BB detection with the LOD value down to 20 fM (Huang et al., 2016b).

In addition, non-enzymatic sensing was also explored using composites consisting of carbon nanomaterials and TMD NSs. For instance, Huang group investigated a composite composed of layered MoS_2 and graphene as a sensing platform for the electrochemical detection of acetaminophen (AC) (Huang et al., 2013b). The electrochemical signal stemed from the AC-involved redox reaction (Equation (6)).

$$\text{Acetaminophen} \leftrightarrow \text{N-acetyl-p-quinoneimine} + 2H^+ + 2e^- \quad (6)$$

The MoS_2/graphene composite-modified GCE exhibited more favorable electron transfer kinetics in comparison with neat GCE and graphene-modified GCE due to the robust composite structure and the synergies between MoS_2 and graphene.

4.2.1.3. Polymer as the modifier. Conducting polymers are also regarded as an alternative to providing a direct path for electrons in the TMD NSs-based electrochemical biosensors. For example, self-doped polyaniline (PANI) has been investigated to modify MoS_2 NSs, yielding a MoS_2/PANI nanocomposite which was used as a sensing platform for the chloramphenicol (CAP) detection. The negatively charged PANI with abundant benzene rings could strongly interact with conjugate-structured CAP, contributing to the excellent electrocatalytic activity for the CAP detection, with a linear range of 0.1–1000 μM and the LOD value of 6.5×10^{-2} μM (Yang et al., 2015a).

4.2.1.4. Modification by multicomponent reactions. To exploit the inherent advantages of different kinds of functional components in a TMDs-based biosensor, TMDs-based ternary composites have also been investigated. For example, Huang group employed both CNTs and Au NPs to hybridize with MoS_2 NSs for the enzymatic detection of DNA using GOx as the enzyme (Huang et al., 2014b). The multicomponent synergies and multiple signal amplification contributed to an ultrasensitive electrochemical detection of DNA with the LOD value down to 0.79 fM and a wide linear range from 10 to 10^7 fM. Later, they fabricated a MoS_2/PANI/Au NPs ternary composite for the non-enzymatic detection of dopamine (DA) (Huang et al., 2014d). The MoS_2/PANI composite film served as an accelerator for electron transfer from DA to the electrode, and the redox-active PANI possessed highly electrolytic accessible surface area after coating on the surface of the MoS_2 NSs. The subsequent deposition of Au NPs onto the surface of the MoS_2/PANI composite further promoted the electron transfer for this redox system (as evidenced by CV, DPV, and ESI), greatly improving the sensing performance. Furthermore, a dual signal amplification was also evidenced in WS_2/graphene/Au NPs ternary composites which were demonstrated with high sensitivity to DNA (down to femtomolar level) and good selectivity to differentiate single-base mismatched and three-base mismatched sequences of DNA (Huang et al., 2014a).

4.2.1.5. Applications in the dual-target detection. Single target (e.g., a protein or a small biomolecule) was frequently investigated for the examination of the established electrochemical sensing system in the mode of "signal-on" or "signal-off". Such a single target detection relies on only one signal variation, which might cause misreading in a multiplex detection system due to the false negative or positive results. In this regard, Su et al. reported a MoS_2/Au NPs composite-based electrochemical sensor capable of individually and simultaneously detecting thrombin and adenosine triphosphate (ATP) as representatives of a small biomolecule and a protein, respectively (Fig. 4a) (Su et al., 2016). Briefly, two different aptamer probes with the hairpin and double-strand structures were labeled with methylene blue (MB) and Ferrocene (Fc), respectively. Both of the probes could be simultaneously immobilized on the MoS_2/Au NPs composite via Au-S bonding. Incubation with thrombin and ATP induced MB and Fc to be far away from ("signal-on") and close to ("signal-off") the electrode surface respectively. This aptasensor possessed both of the features of "signal-off" and "signal-on" sensing mechanisms, resulting in high sensitivity, with few misreadings (see Table 1 for more details).

4.2.2. Photoelectrochemical (PEC)-based

The semiconducting TMD NSs have also been employed as a photocatalyst for PEC-based sensing applications under visible light (Fig. 4b). Compared to the electrochemical biosensing, the sensitivity of the PEC biosensing can be further improved, along with a low background signal, due to the total separation of the excitation source (i.e., visible or solar light) and the detection signal (i.e., photocurrent) and to the different energy forms of the excitation source and the detection signal. For example, MoS_2 NSs, with a direct bandgap of ~1.85 eV, were used for the PEC detection of glucose under visible light through injection of the glucose solutions with various concentrations into the electrolyte, achieving excellent PEC sensing performance (linear range: 8 nM-5 μM; LOD: ~0.6 nM) (Wu et al., 2017).

4.2.3. FETs-based

FETs-based biosensing has also captivated much attention, in that inexpensive, rapid, portable, and label-free detection can be achieved. The on-chip integration of both sensor and measurement systems can be easily realized as well. Using 2D TMDs as an active channel material in the FET-based electronic biosensors has attracted substantial interest (Lee et al., 2013; Yadav et al., 2019). To construct a FET-based biosensor, the physical gate in a logic transistor is removed, and the dielectric layer is modified with specific receptors for capturing the desired target biomolecules in a highly selective manner (Fig. 5a). Once the charged biomolecules are captured, a gating (electrostatic) effect will be produced, which is further transduced into a readable signal in the form of variation in the FET electrical characteristics such as channel conductance or drain-to-source current. MoS_2 NSs were demonstrated to be an excellent channel material for the fabrication of high-performance FET biosensors, due to their semiconducting and atomically thin 2D nature (Sarkar et al., 2014). A superior electrostatic gating effect endowed a MoS_2-included FET device with a high protein sensitivity of 196 even at the 100 fM concentration (left part of Fig. 5a).

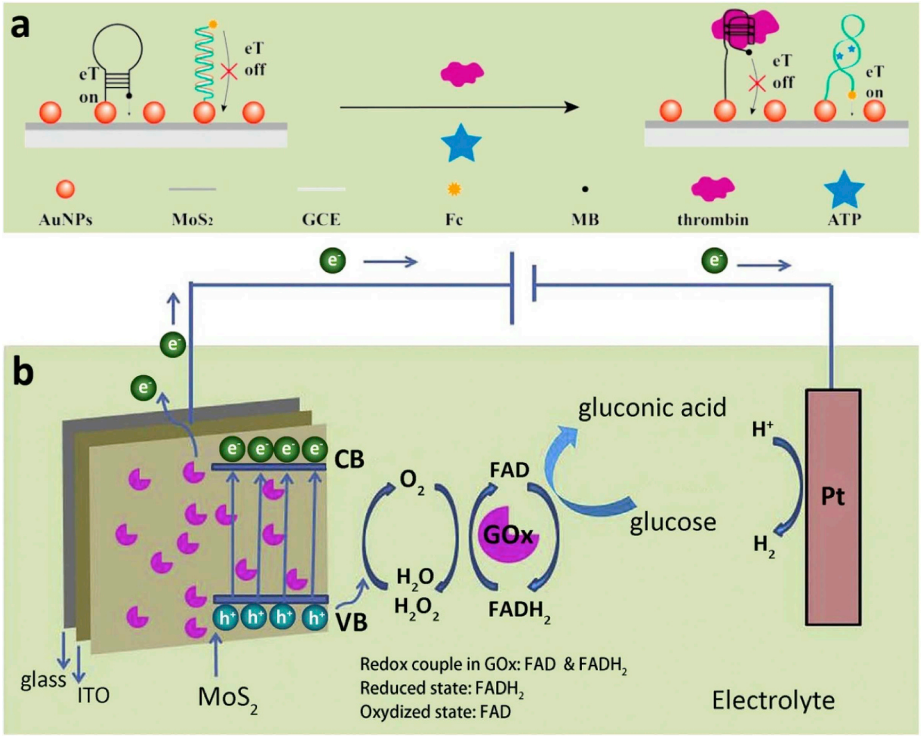

Fig. 4. a) Scheme of an aptasensor for the simultaneous determination of dual targets (ATP and thrombin). Reproduced with permission from (Su et al., 2016). Copyright 2016, American Chemical Society. b) Presentation of the PEC reaction process of the MoS_2-GOx-modified ITO electrode for the detection of glucose. Reproduced with permission from (Wu et al., 2017). Copyright 2017, Elsevier.

Thereafter, high-quality MoS_2 NSs (highly stable in electrolytes and inert to pH changes) were also used as the channel material for the FET-based label-free detection of DNA (Lee et al., 2015). The hybridization of the probe ssDNA with the target ssDNA resulted in the detachment of the probe ssDNA from the MoS_2 surface, accompanied by the generation of an electrostatic gating effect, enabling a negative shift in the threshold voltage and an enhancement in the drain current. Fig. 5b presents a schematic illustration of the MoS_2-based FET configuration, along with the plot of the threshold voltage shifts ($\triangle V_{th}$) vs. the concentrations of complementary, non-complementary and single-base mismatched DNA. An excellent sensing performance was achieved (LOD: 10 fM; sensitivity: 17 mV/dec; dynamic range: 10^6). To avoid the sensitivity lowered by the membrane that is inevitably involved in traditional semiconductor-based FETs, a membraneless FET was investigated with WSe_2 as the channel material for the glucose detection. Defect-free WSe_2 surface without dangling bonds was an essential condition for the effective fabrication of such a membraneless FET with high sensitivity since there would be nonspecific bindings as caused by the surface detects (Lee et al., 2018). Nonetheless, the low-power O_2 plasma treatment of the defect-free WSe_2 surface was also necessary to create some binding sites for the bioreceptors and thus to obtain high reusability and stability of the FET-based biosensor, as shown in Fig. 5c.

5. Conclusion and future perspectives

This work has comprehensively investigated the state-of-the-art contributions to the fabrication, manipulation, and biosensing applications of 2D TMDs-based systems for the detection of various bioanalytes. Overwhelmingly more attention has been paid to 2D MoS_2 as compared to the other 2D TMDs, likely due to its relatively better studied optical and electronic properties. It is therefore highly desirable to put more focus on the other 2D TMDs to develop novel biosensors for addressing the current bottleneck encountered by 2D MoS_2. In addition, using TMDs-based nanocomposites to construct biosensors has been widely investigated to address the drawback existing in pristine TMDs, such as the poor electronic conductivity, but the components are usually limited to conducting polymers, carbon nanomaterials, and noble metal NPs (Table 1). It should have great potentials to capitalize other kinds of functional components such as non-precious metals, semiconductors (e.g., TiO_2, ZnO_2, CdS, etc), perovskite and MOF, for the fabrication of diverse novel high-performance biosensors.

Although big progress has been made in the preparation of various TMDs-based biosensors for a wide range of bioanalytes including proteins, DNA, small biomolecules, there still exists a big room for the further improvement of the sensitivity of the biosensors. On the other hand, the widespread applications of 2D TMDs-based fluorimetric biosensors were limited by the fact that the fluorophore-labeled method causes the sensing assays to be complex, high-cost, and time-consuming. Therefore, label-free approaches based on 2D TMDs are encouraged with more attention. Other than sensitivity and concentration range parameters, there are currently limited reports on the investigation of the selectivity and stability of 2D TMDs-based biosensors. It merits to pay special attention on these parameters in 2D TMDs-based biosensors given that they have been widely investigated for non-2D materials.

Scalable methods for the fabrication of 2D TMDs and their nanocomposites remain lacking from the practical application viewpoint, as most of the reported 2D TMDs-based biosensors are fabricated under laboratory conditions. Therefore, effective and efficient techniques still remain to be explored for the rapid production of biosensors based on TMD NSs and their nanocomposites in large quantities and with high-quality specifications, while maintaining a relatively low cost. This is a prerequisite for the commercialization of TMDs-based biosensors. More efforts should also be devoted to bringing TMD-based biosensing systems to the real-world applications since the biosensor showing good performance under the optimized laboratory conditions is most likely to perform unsatisfactorily for the practical applications involving many interfering species such as mixed ions, particles, and macromolecules that would produce many interfering signals during the detection. Considering the explosively growing experimental findings and the rapid development of the supporting technologies, we believe that the 2D TMDs-based biosensors will eventually become eye-catching products for overcoming various challenges in the modern biosensing world.

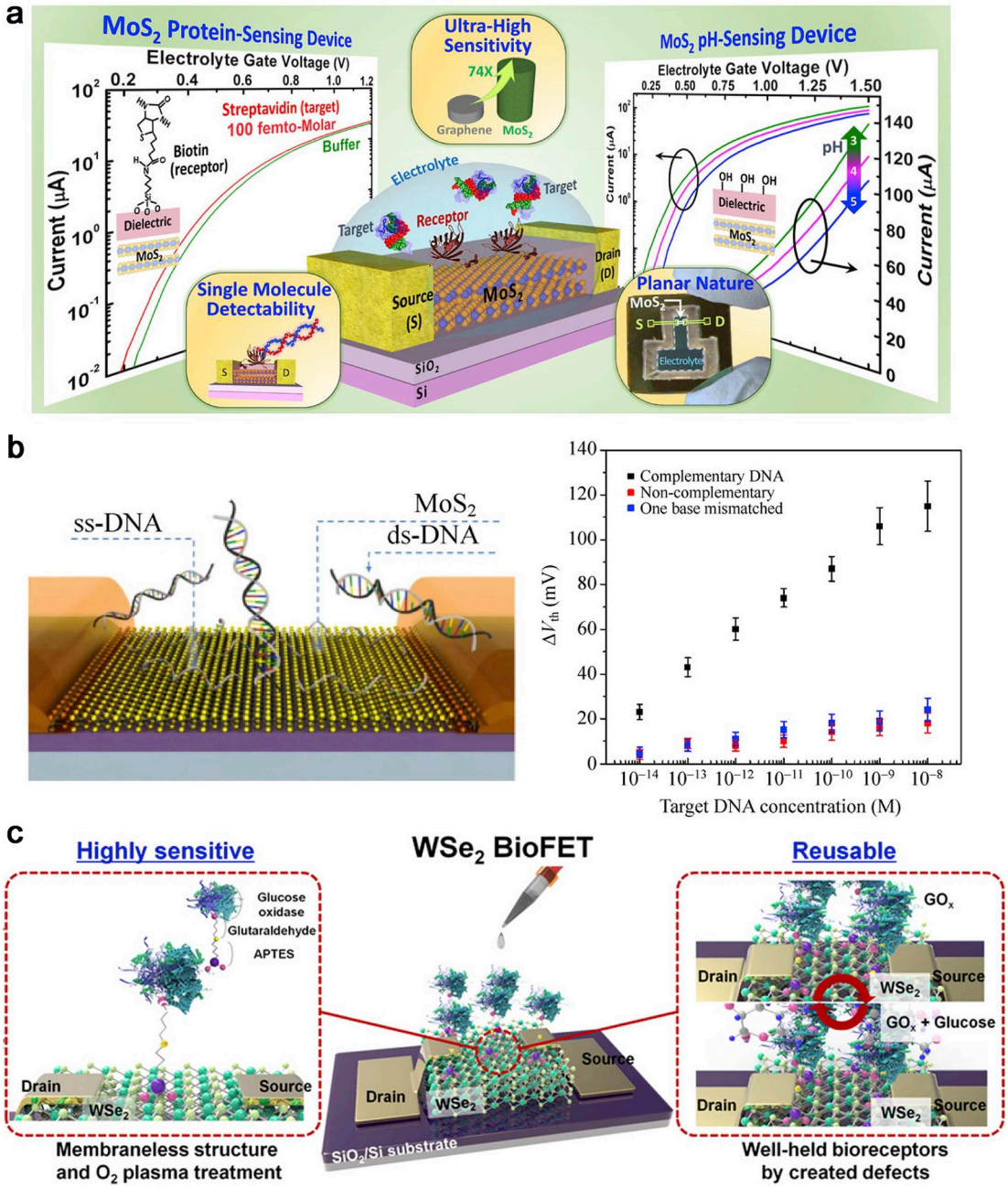

Fig. 5. a) Scheme of a MoS_2-based FET biosensor. The dielectric layer covering the MoS_2 channel is modified with receptors for specifically binding with the target biomolecules. The uptake of the charged biomolecules induces a gating effect, enabling the modulation of the device current. An electrolyte gate in the form of an Ag/AgCl reference electrode is employed for applying a bias to the electrolyte. The FET biosensor exhibited double performances for sensing both protein (i.e., streptavidin) and pH. Reproduced with permission from (Sarkar et al., 2014). Copyright 2014, American Chemical Society. b) Schematic illustration of the MoS_2 FET configuration (left panel), and plots of the dependency of $\triangle V_{th}$ on the concentration of complementary, non-complementary and single-base mismatched DNA molecules (right panel). Reproduced with permission from (Lee et al., 2015). Copyright 2015, Springer. c) Illustration of constructing a WSe_2-based membraneless bio-FET for the enzymatic detection of glucose (the left and right parts show the composition of the bio-FET and the reusability of the bio-FET for glucose detection, respectively). Reproduced with permission from (Lee et al., 2018). Copyright 2018, American Chemical Society.

CRediT authorship contribution statement

Huawen Hu: Writing - original draft, Writing - review & editing, Funding acquisition. **Ali Zavabeti:** Writing - review & editing. **Haiyan Quan:** Resources. **Wuqing Zhu:** Resources. **Hongyang Wei:** Resources. **Dongchu Chen:** Writing - review & editing. **Jian Zhen Ou:** Validation, Funding acquisition, Writing - review & editing.

Acknowledgments

We gratefully appreciate the National Natural Science Foundation of China (51702050), the Featured Innovation Project of the Department of Education of Guangdong Province (2017KTSCX188), the Open Research Foundation of Guangdong Provincial Key Laboratory of New and Renewable Energy Research and Development (Y807s31001), and

the Open Research Foundation of Guangdong Provincial Key Laboratory of Industrial Surfactant (GDLS-01-2019). J. Z. Ou and A. Zavabeti also acknowledge the financial support from the Australian Research Council (DE160100715, CE170100039 and DP180102752).

Appendix A. Supplementary data

Supplementary data to this article can be found online at https://doi.org/10.1016/j.bios.2019.111573.

References

Appel, J.H., Li, D.O., Podlevsky, J.D., Debnath, A., Green, A.A., Wang, Q.H., Chae, J., 2016. ACS Biomater. Sci. Eng. 2 (3), 361–367.
Bollella, P., Fusco, G., Tortolini, C., Sanzò, G., Favero, G., Gorton, L., Antiochia, R., 2017. Biosens. Bioelectron. 89, 152–166.
Chao, J., Han, X., Sun, H., Su, S., Weng, L., Wang, L., 2015a. Sci. China Chem. 59 (3), 332–337.
Chao, J., Zou, M., Zhang, C., Sun, H., Pan, D., Pei, H., Su, S., Yuwen, L., Fan, C., Wang, L., 2015b. Nanotechnology 26 (27), 274005.
Chng, E.L.K., Pumera, M., 2015. RSC Adv. 5 (4), 3074–3080.
Chng, E.L.K., Sofer, Z., Pumera, M., 2014. Nanoscale 6 (23), 14412–14418.
Chow, P.K., Jacobs-Gedrim, R.B., Gao, J., Lu, T.-M., Yu, B., Terrones, H., Koratkar, N., 2015. ACS Nano 9 (2), 1520–1527.
Dou, B., Yang, J., Yuan, R., Xiang, Y., 2018. Anal. Chem. 90 (9), 5945–5950.
Du, C., Shang, A., Shang, M., Ma, X., Song, W., 2018. Sens. Actuators B Chem. 255, 926–934.
Fahimi-Kashani, N., Rashti, A., Hormozi-Nezhad, M.R., Mahdavi, V., 2017. Anal. Methods 9 (4), 716–723.
Fang, L.-X., Cao, J.-T., Huang, K.-J., 2015. J. Electroanal. Chem. 746, 1–8.
Fang, L., Wang, F., Chen, Z., Qiu, Y., Zhai, T., Hu, M., Zhang, C., Huang, K., 2017. Talanta 167, 593–599.
Feng, Q., Zhu, Y., Hong, J., Zhang, M., Duan, W., Mao, N., Wu, J., Xu, H., Dong, F., Lin, F., Jin, C., Wang, C., Zhang, J., Xie, L., 2014. Adv. Mater. 26 (17), 2648–2653 2613.
Ge, J., Ou, E.-C., Yu, R.-Q., Chu, X., 2014a. J. Mater. Chem. B 2 (6), 625–628.
Ge, J., Tang, L.-J., Xi, Q., Li, X.-P., Yu, R.-Q., Jiang, J.-H., Chu, X., 2014b. Nanoscale 6 (12), 6866–6872.
Gu, W., Yan, Y., Zhang, C., Ding, C., Xian, Y., 2016. ACS Appl. Mater. Interfaces 8 (18), 11272–11279.
Han, K.H., Kim, J.Y., Jo, S.G., Seo, C., Kim, J., Joo, J., 2017. Nanotechnology 28 (43), 435501.
Hao, J., Song, G., Liu, T., Yi, X., Yang, K., Cheng, L., Liu, Z., 2017a. Adv. Sci. 4 (1).
Hao, L., Gu, H., Duan, N., Wu, S., Ma, X., Xia, Y., Tao, Z., Wang, Z., 2017b. Anal. Chim. Acta 959, 83–90.
Hu, H., Xin, J., Hu, H., Wang, X., Lu, X., 2014. Molecules 19 (6), 7459–7479.
Huang, J., Dong, Z., Li, Y., Li, J., Tang, W., Yang, H., Wang, J., Bao, Y., Jin, J., Li, R., 2013a. Mater. Res. Bull. 48 (11), 4544–4547.
Huang, K.-J., Liu, Y.-J., Wang, H.-B., Gan, T., Liu, Y.-M., Wang, L.-L., 2014a. Sens. Actuators B Chem. 191, 828–836.
Huang, K.-J., Liu, Y.-J., Wang, H.-B., Wang, Y.-Y., Liu, Y.-M., 2014b. Biosens. Bioelectron. 55, 195–202.
Huang, K.-J., Liu, Y.-J., Zhang, J.-Z., Liu, Y.-M., 2014c. Anal. Methods 6 (19), 8011–8017.
Huang, K.-J., Shuai, H.-L., Chen, Y.-X., 2016a. Sens. Actuators B Chem. 225, 391–397.
Huang, K.-J., Shuai, H.-L., Zhang, J.-Z., 2016b. Biosens. Bioelectron. 77, 69–75.
Huang, K.-J., Wang, L., Li, J., Liu, Y.-M., 2013b. Sens. Actuators B Chem. 178, 671–677.
Huang, K.-J., Zhang, J.-Z., Liu, Y.-J., Wang, L.-L., 2014d. Sens. Actuators B Chem. 194, 303–310.
Kalantar-zadeh, K., Ou, J.Z., 2015. ACS Sens. 1 (1), 5–16.
Kaur, J., Singh, M., Dell'Aversana, C., Benedetti, R., Giardina, P., Rossi, M., Valadan, M., Vergara, A., Cutarelli, A., Montone, A.M.I., Altucci, L., Corrado, F., Nebbioso, A., Altucci, C., 2018. Sci. Rep. 8 (1).
Kaushik, S., Tiwari, U.K., Deep, A., Sinha, R.K., 2019. Sci. Rep. 9 (1), 6987.
Kaushik, S., Tiwari, U.K., Pal, S.S., Sinha, R.K., 2018. Biosens. Bioelectron. 126 (1), 501–509.
Kenry, Lim, C.T., 2017. ChemNanoMat 3 (1), 5–16.
Khataee, A., Haddad Irani-nezhad, M., Hassanzadeh, J., Woo Joo, S., 2018. J. Colloid Interface Sci. 515, 39–49.
Lan, L., Yao, Y., Ping, J., Ying, Y., 2019. Sens. Actuators B Chem. 290, 565–572.
Lee, D.-W., Lee, J., Sohn, I.Y., Kim, B.-Y., Son, Y.M., Bark, H., Jung, J., Choi, M., Kim, T.H., Lee, C., Lee, N.-E., 2015. Nano Res. 8 (7), 2340–2350.
Lee, H.W., Kang, D.-H., Cho, J.H., Lee, S., Jun, D.-H., Park, J.-H., 2018. ACS Appl. Mater. Interfaces 10 (21), 17639–17645.
Lee, K., Gatensby, R., McEvoy, N., Hallam, T., Duesberg, G.S., 2013. Adv. Mater. 25 (46), 6699–6702.
Li, B.L., Zou, H.L., Lu, L., Yang, Y., Lei, J.L., Luo, H.Q., Li, N.B., 2015. Adv. Funct. Mater. 25 (23), 3541–3550.
Li, J., Zhao, Q., Tang, Y., 2016. Sensors 16 (6), 865.
Li, X., Du, X., 2017. Sens. Actuators B Chem. 239, 536–543.
Lin, T., Zhong, L., Guo, L., Fu, F., Chen, G., 2014a. Nanoscale 6 (20), 11856–11862.
Lin, T., Zhong, L., Song, Z., Guo, L., Wu, H., Guo, Q., Chen, Y., Fu, F., Chen, G., 2014b. Biosens. Bioelectron. 62, 302–307.
Lin, X., Ni, Y., Kokot, S., 2016. Biosens. Bioelectron. 79, 685–692.
Liu, X., Ge, J., Wang, X., Wu, Z., Shen, G., Yu, R., 2014. Anal. Methods 6 (18), 7212–7217.
Liu, X., Shuai, H.-L., Liu, Y.-J., Huang, K.-J., 2016. Sens. Actuators B Chem. 235, 603–613.
Loan, P.T., Zhang, W., Lin, C.T., Wei, K.H., Li, L.J., Chen, C.H., 2014. Adv. Mater. 26 (28), 4838–4844.
Lu, C., Liu, Y., Ying, Y., Liu, J., 2017. Langmuir 33 (2), 630–637.
Mani, S., Ramaraj, S., Chen, S.M., Dinesh, B., Chen, T.W., 2017. J. Colloid Interface Sci. 507, 378–385.
Maurya, J.B., Prajapati, Y.K., Singh, V., Saini, J.P., Tripathi, R., 2015. Opt. Quant. Electron. 47 (11), 3599–3611.
Mishra, A.K., Mishra, S.K., Verma, R.K., 2016. J. Phys. Chem. C 120 (5), 2893–2900.
Nandwana, V., Huang, W., Li, Y., Dravid, V.P., 2018. ACS Appl. Nano Mater. 1 (4), 1949–1958.
Nasir, M.Z.M., Mayorga-Martinez, C.C., Sofer, Z., Pumera, M., 2017. ACS Nano 11 (6), 5774–5784.
Naveen, M.H., Gurudatt, N.G., Noh, H.-B., Shim, Y.-B., 2016. Adv. Funct. Mater. 26 (10), 1590–1601.
Nirala, N.R., Vinita, Prakash, R., 2018. Microchim. Acta 185 (4).
Ouyang, Q., Zeng, S., Jiang, L., Hong, L., Xu, G., Dinh, X.Q., Qian, J., He, S., Qu, J., Coquet, P., Yong, K.T., 2016. Sci. Rep. 6, 28190.
Pathania, P.K., Saini, J.K., Vij, S., Tewari, R., Sabherwal, P., Rishi, P., Suri, C.R., 2018. Biosens. Bioelectron. 122, 121–126.
Qin, Y., Ma, Y., Jin, X., Zhang, L., Ye, G., Zhao, S., 2015. Anal. Chim. Acta 866, 84–89.
Rahmanian, E., Mayorga-Martinez, C.C., Malekfar, R., Luxa, J., Sofer, Z., Pumera, M., 2018. ACS Appl. Nano Mater. 1 (12), 7006–7015.
Sarkar, D., Liu, W., Xie, X., Anselmo, A.C., Mitragotri, S., Banerjee, K., 2014. ACS Nano 8 (4), 3992–4003.
Sarkar, D., Xie, X., Kang, J., Zhang, H., Liu, W., Navarrete, J., Moskovits, M., Banerjee, K., 2015. Nano Lett. 15 (5), 2852–2862.
Selvarani, K., Prabhakaran, A., Arumugam, P., Berchmans, S., Nayak, P., 2018. Microchim. Acta 185 (9).
Shuai, H.-L., Huang, K.-J., Chen, Y.-X., 2016. J. Mater. Chem. B 4 (6), 1186–1196.
Song, H., Ni, Y., Kokot, S., 2014. Biosens. Bioelectron. 56, 137–143.
Su, S., Sun, H., Cao, W., Chao, J., Peng, H., Zuo, X., Yuwen, L., Fan, C., Wang, L., 2016. ACS Appl. Mater. Interfaces 8 (11), 6826–6833.
Su, S., Sun, H., Xu, F., Yuwen, L., Fan, C., Wang, L., 2014. Microchim. Acta 181 (13–14), 1497–1503.
Su, S., Sun, H., Xu, F., Yuwen, L., Wang, L., 2013. Electroanalysis 25 (11), 2523–2529.
Sun, X., Liu, Z., Welsher, K., Robinson, J.T., Goodwin, A., Zaric, S., Dai, H., 2008. Nano Res. 1 (3), 203–212.
Tan, C., Yu, P., Hu, Y., Chen, J., Huang, Y., Cai, Y., Luo, Z., Li, B., Lu, Q., Wang, L., Liu, Z., Zhang, H., 2015. J. Am. Chem. Soc. 137 (32), 10430–10436.
Teo, W.Z., Chng, E.L.K., Sofer, Z., Pumera, M., 2014. Chem. Eur J. 20 (31), 9627–9632.
Thanh, T.D., Chuong, N.D., Hien, H.V., Kshetri, T., Tuan, L.H., Kim, N.H., Lee, J.H., 2018. Prog. Mater. Sci. 96, 51–85.
Toh, R.J., Mayorga-Martinez, C.C., Han, J., Sofer, Z., Pumera, M., 2017. Anal. Chem. 89 (9), 4978–4985.
Vovusha, H., Sanyal, B., 2015. RSC Adv. 5 (83), 67427–67434.
Wang, G.-X., Bao, W.-J., Wang, J., Lu, Q.-Q., Xia, X.-H., 2013a. Electrochem. Commun. 35, 146–148.
Wang, L., Wang, Y., Wong, J.I., Palacios, T., Kong, J., Yang, H.Y., 2014a. Small 10 (6), 1101–1105.
Wang, S., Zhang, S., Liu, M., Song, H., Gao, J., Qian, Y., 2018. Sens. Actuators B Chem. 254, 1101–1109.
Wang, T., Zhu, H., Zhuo, J., Zhu, Z., Papakonstantinou, P., Lubarsky, G., Lin, J., Li, M., 2013b. Anal. Chem. 85 (21), 10289–10295.
Wang, T., Zhu, R., Zhuo, J., Zhu, Z., Shao, Y., Li, M., 2014b. Anal. Chem. 86 (24), 12064–12069.
Wang, X., Chu, C., Shen, L., Deng, W., Yan, M., Ge, S., Yu, J., Song, X., 2015. Sens. Actuators B Chem. 206, 30–36.
Wang, Y.-H., Huang, K.-J., Wu, X., 2017. Biosens. Bioelectron. 97, 305–316.
Wu, S., Huang, H., Shang, M., Du, C., Wu, Y., Song, W., 2017. Biosens. Bioelectron. 92, 646–653.
Wu, S., Zeng, Z., He, Q., Wang, Z., Wang, S.J., Du, Y., Yin, Z., Sun, X., Chen, W., Zhang, H., 2012. Small 8 (14), 2264–2270.
Xiang, X., Shi, J., Huang, F., Zheng, M., Deng, Q., Xu, J., 2015. Biosens. Bioelectron. 74, 227–232.
Yadav, V., Roy, S., Singh, P., Khan, Z., Jaiswal, A., 2019. Small 15 (1), 1803706.
Yang, J.-K., Lee, H.-R., Hwang, I.-J., Kim, H.-I., Yim, D., Kim, J.-H., 2018. Adv. Healthc. Mater. 7 (14), 1701496.
Yang, R., Zhao, J., Chen, M., Yang, T., Luo, S., Jiao, K., 2015a. Talanta 131, 619–623.
Yang, T., Chen, M., Nan, F., Chen, L., Luo, X., Jiao, K., 2015b. J. Mater. Chem. B 3 (24), 4884–4891.
Yang, T., Yang, R., Chen, H., Nan, F., Ge, T., Jiao, K., 2015c. ACS Appl. Mater. Interfaces 7 (4), 2867–2872.
Zeng, S., Hu, S., Xia, J., Anderson, T., Dinh, X.-Q., Meng, X.-M., Coquet, P., Yong, K.-T., 2015. Sens. Actuators B Chem. 207, 801–810.
Zhang, Y., Zheng, B., Zhu, C., Zhang, X., Tan, C., Li, H., Chen, B., Yang, J., Chen, J., Huang, Y., Wang, L., Zhang, H., 2015. Adv. Mater. 27 (5), 935–939.
Zhao, J., Jin, X., Vdovenko, M., Zhang, L., Sakharov, I.Y., Zhao, S., 2015. Chem. Commun. 51 (55), 11092–11095.
Zhu, C., Zeng, Z., Li, H., Li, F., Fan, C., Zhang, H., 2013. J. Am. Chem. Soc. 135 (16), 5998–6001.